Magn Reson Mater Phy
DOI 10.1007/s10334-011-0284-5

RESEARCH ARTICLE

# Possibilities and limitations for high resolution small animal MRI on a clinical whole-body 3T scanner

**Karl-Heinz Herrmann · Silvio Schmidt · Alexandra Kretz · Ronny Haenold · Ines Krumbein · Martin Metzler · Christian Gaser · Otto W. Witte · Jürgen R. Reichenbach**

Received: 17 June 2011 / Revised: 16 August 2011 / Accepted: 13 September 2011


**Abstract**
*Object* To investigate the potential of a clinical 3 T scanner to perform MRI of small rodents.
*Materials and methods* Different dedicated small animal coils and several imaging sequences were evaluated to optimize image quality with respect to SNR, contrast and spatial resolution. As an application, optimal grey-white-matter contrast and resolution were investigated for rats. Furthermore, manganese-enhanced MRI was applied in mice with unilateral crush injury of the optic nerve to investigate coil performance on topographic mapping of the visual projection.
*Results* Differences in SNR and CNR up to factor 3 and more were observed between the investigated coils. The best grey-white matter contrast was achieved with a high resolution 3D $T_2$-weighted TSE (SPACE) sequence. Delineation of the retino-tectal projection and detection of defined visual pathway damage on the level of the optic nerve could be achieved by using a $T_1$-weighted, 3D gradient echo sequence with isotropic resolution of $(0.2\ \text{mm})^3$.
*Conclusions* Experimental studies in small rodents requiring high spatial resolution can be performed by using a clinical 3 T scanner with appropriate dedicated coils.

**Keywords** MRI · Rodents · Clinical scanner · High spatial resolution · 3 T · Morphometry · MEMRI

## Introduction

High resolution MRI of small animals, such as mice and rats, is increasingly applied in experimental neurological and neuroscientific studies to investigate brain injuries or brain plasticity as well as to monitor volume changes or drug treatment longitudinally over time in the same animal. Dedicated ultra-high field animal scanners allow MR imaging with impressively high spatial resolution (on the order of 30 μm or even higher) in combination with excellent soft tissue contrast [1]. However, many laboratories and clinical research groups do not have easy access to dedicated animal systems, whereas clinical whole-body scanners are often more easily available [2]. Indeed, clinical scanners provide several advantages, including well-established optimised clinical protocols with sequences that sometimes do not have corresponding, directly available counterparts on animal scanners. Additionally, field strength influences the tissue contrast, e.g. due to changes in $T_1$ and $T_2$ relaxation times, and animal imaging at clinical field strengths is therefore closer to human imaging. Also, the contrast generating effects of many $T_1$-shortening agents, like for example Gd-DTPA, are reduced at ultra-high field strengths. The large bore size of human scanners and, thus, the facilitated access to the

K.-H. Herrmann (✉) · I. Krumbein · J. R. Reichenbach
Medical Physics Group, Institute for Diagnostic and Interventional Radiology I, Jena University Hospital, Philosophenweg 3, Gebäude 5, 07743 Jena, Germany
e-mail: karl-heinz.herrmann@med.uni-jena.de

S. Schmidt · A. Kretz · M. Metzler · C. Gaser · O. W. Witte
Hans Berger Department of Neurology, Jena University Hospital, Erlanger Allee 101, 07747 Jena, Germany

R. Haenold
Leibniz Institute for Age Research, Fritz Lipmann Institute, Beutenberger Str.11, 07745 Jena, Germany

C. Gaser
Department of Psychiatry , Jena University Hospital, Philosophenweg 3, 07743 Jena, Germany

Published online: 22 October 2011

animal and space for necessary equipment can also be advantageous in some applications.

However, to enable and improve small animal imaging on clinical scanners, dedicated hardware has to be used. On the one hand, extensions to the hardware may consist of sophisticated upgrade equipment, such as gradient insert coils [3], which require integration into the scanner system and are, consequently, quite costly. On the other hand, good image quality can already be achieved using commercially available, standard small loop coils in combination with the standard gradient system of a whole-body scanner [4]. By now, a number of suitable small clinical coils as well as dedicated small animal coils are available, including simple loop coils, multi-channel surface coils or volume resonators, which, in combination with clinical high-field MRI systems, can produce excellent image quality within reasonable scan time.

### Hardware limitations on clinical scanners

Even with a good selection of coils available, there remain major differences between animal scanners and clinical whole body scanners, which influence image quality and spatial resolution. The lower $B_0$ field strength of clinical scanners (typically 1–3 T) is inherently associated with a reduced signal-to-noise-ratio (SNR) compared to animal scanners (4.7–11.7 T and even higher). This SNR reduction is a fundamental restriction, but can be partially compensated at the expense of spatial resolution. For instance, increasing all three voxel dimensions by 25% compensates for a difference of factor 2 in field strength. Signal averaging can also counterbalance the lower SNR at low field strengths.

A more serious problem is the distinctly lower gradient strength and gradient slew rate available on clinical systems. With typical gradient strengths of 40 mT/m and slew rates up to 200 T/m/s compared to gradients of 700–1,000 mT/m and slew rates of up to 5,000 T/m/s on state-of-the-art animal scanners, these hardware limitations not only restrict the minimum slice thickness, but also the minimal field-of-view (FoV). Consequently, clinical scanners will not be able to compete for resolution with dedicated small animal systems.

Especially for functional and diffusion MRI, in combination with the commonly used echo planar imaging (EPI), the low gradient strength and slew rates of a clinical scanner make it difficult to acquire these types of contrasts in sufficient resolution and image quality for rats and close to impossible for mice. The primary issue is, that for very small FoVs the limited gradients necessitate very long readouts and thereby lenghten the echo train. This causes longer effective echo times, more signal loss and severe distortions in the EPI images. Additionally, to reduce geometric distortions and intra voxel signal decay, EPI requires a very good shim which, especially for mice, can not be provided by a clinical shim system. Accurate transmitter voltage adjustment can also become challenging for very small objects, particularly if the scanner's body coil is used for transmitting. Nevertheless, for anatomical imaging, using 3D acquisitions instead of 2D slice selective acquisitions, an isotropic resolution of $(0.2\ \text{mm})^3$ is technically feasible on clinical 3 T scanners, provided that sufficient measurement time can be afforded in the particular experiment to obtain acceptable SNR and image quality.

### Aims

The aims of this study were to evaluate image quality and achievable spatial resolution on a clinical whole body 3 T scanner using different small coils and a variety of optimised MR sequences. Image quality was assessed by evaluating two animal models. In the first model, grey and white matter contrast was optimised for rat brain. In the second model, depiction of the visual projection of mice was investigated with manganese enhanced $T_1$-weighted MRI (MEMRI). Signal-to-noise-ratio (SNR) and contrast-to-noise-ratio (CNR) performance of different coils as well as different sequences were compared.

## Material and methods

### MR scanner and coils

All experiments were performed on a clinical 3 T whole-body scanner (Magnetom TIM Trio, Siemens Medical Solutions, Erlangen, Germany). Two small surface coils and two dedicated volume coils for small animal imaging, described in detail below, were used in the different studies:

1. A multi-functional, dual-module, 8-channel surface coil, (Cloth Pin Coil (CPC), Noras MRI products GmbH, Höchberg, Germany), as shown in Fig. 1a [5]. Each of the two modules contains four loop coils (ø 50 mm) in a shamrock configuration with partial overlap. The coil has CE certification for application in humans and is equipped with a highly flexible mounting system that enables rotation and tilt of the two modules as well as rotation and translation of the mounting arms to nearly any required position.
2. A small loop coil (Fig. 1b) with inner diameter of 30 mm (Small Loop (L4), Siemens Healthcare, Erlangen, Germany). This coil has also CE certification for application in humans.
3. An 8-channel, phased-array whole-body mouse coil (Rapid Biomedical GmbH, Rimpar, Germany) with an inner diameter of 35 mm. The array consists of two

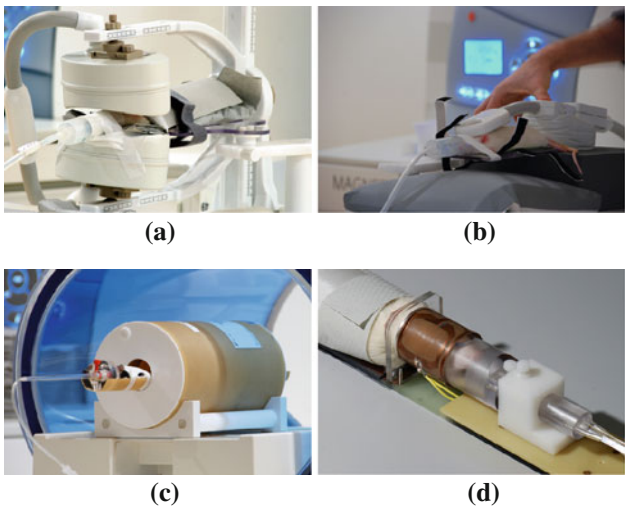


**Fig. 1** Photographs showing coil placement, immobilisation of the animal head and anaesthesia supply. **a** CPC coil in measurement position. The rat's body is placed on the supporting table, its head directly on the lower coil module. **b** Loop surface coil placed in close contact with the rat's head for optimal SNR. Inhalation anaesthetics are supplied through the tube. **c** Whole body 8-channel mouse array. Inhalation anaesthetics are supplied through the tube on the left. **d** Litz coil with modified head mounting for rats. Inhalation anaesthetics are supplied through the tubes on the far right directly to the rat's snout

rings of pentagonally shaped coil elements, offering an effective axial FoV of 100 mm (Fig. 1c).

4. A dedicated rat head coil (Fig. 1d) with a linearly polarised Litz volume resonator design (Doty Scientific Inc., Columbia, SC, USA). With an inner diameter of 38 mm and length of 50 mm the coil provides a homogeneous FoV of 33 mm in axial direction [6]. It operates in transmit-receive mode and allows individually adjustable tune and match for each animal. The complete coil assembly is inserted into a copper coated RF shield tube (ø 10 cm, 100 cm long) for imaging.

Rat experiments were carried out with all coils, except the 8-channel mouse array due to spatial restrictions to accommodate the animal. Since this coil has a "dead zone" of approx. 1 cm at the entrance of the coil, animals have to be inserted deeply into the coil, which is not possible with rats. Experiments with mice were performed with both the 8-channel mouse array and the Litz rat head coil. Only one ring with four coil elements of the 8-channel array was used for mouse brain imaging, since this slightly improved SNR and allowed the same small FoV in axial direction as used for the Litz coil.

## Animal setup

Depending on the coil, animal fixation and supply of anaesthesia was different (Fig. 1). For the CPC and the small loop coil, fixation and anaesthesia supply was performed by a conically deformed tube that fitted over the snout of the rodent and was used for gas delivery (Fig. 1a and b). To ensure minimal head motion despite free breathing of the animal, padding under the chin and around the head was used. A plane table made of plastic material provided stable support for the body. The animal's head was positioned directly on the lower coil module; the second coil module was brought in contact with the head from above as close as possible (Fig. 1a).

The small loop coil (L4) was placed directly on the animal's head. In this case, the anaesthesia tube acted also as a distance holder to avoid exertion of pressure to the head by the coil (Fig. 1b).

The 8-channel mouse coil is equipped with an animal bed, including a head mount (Fig. 1c). For the Litz rat head coil, the mounting and head holder were custom built (Fig. 1d) in two different sizes for rats and mice. These head holders all work by the same principle: After locking the front teeth of the rodent in a bite bar, the animal's head is then pulled into the conically shaped front part of the holder. The head holder allows free and unrestricted breathing of the animal, while immobilising the animal's head effectively at the same time. In particular, it prevents nutational movements, which are commonly caused by breathing.

Anaesthesia was provided by an isoflurane vaporizer placed outside the RF cabin of the scanner. A gas mixture of 1.75% isoflurane with oxygen was used for rats and mice. To prevent hypothermia during imaging the animals were wrapped in tissue paper for thermal insulation. Rectal temperature was monitored using a Fluotemp converter type FTC-DIN-ST-LS and Fluotemp fibre optic temperature sensor type FTP-LN2-ST1 (Photon Control Inc, Burnaby BC, Canada). Respiration was monitored using an in-house developed optical motion sensor [7]. However, a variety of systems based on pressure sensors are commercially available and easy to use. Care was taken to position the animals close to the isocenter of the magnet. When using the CPC or the small loop coil, an RF cushion with a high dielectric constant and low conductivity was placed in the vicinity of the coil to facilitate transmitter adjustment. When performing experiments with mice and using the 8-channel phased-array coil, the homogeneity of the excitation field was improved by placing the complete coil setup into the scanner vendor's body load phantom (see Fig. 1c). The Litz coil was placed inside a shielding tube without additional load since this coil was operated in transmit-receive mode. The automatic transmitter adjustment resulted in a typical reference voltage of 4–6 V for mice and 7–9 V for rats.

Since the automatic shim procedure of the scanner is not suited to very small objects the scanner's default shim (tune up) was used. Careful placing of the object in the

isocenter allowed easy automatic frequency and transmit adjustment for rats. However, for mice a prior manual shim adjustment of the linear axial component was necessary to compensate for a strong $B_0$ inhomogeneity caused by the mouse's anatomy. After creating a single peak in the frequency response, automatic frequency and transmitter adjustment were successfully performed by the scanner.

## MRI sequences

Many imaging applications require excellent grey and white matter contrast with high CNR and SNR. For example, deformation or voxel-based volumetry [8, 9] represent applications, for which this internal grey-white contrast is essential. The use of isotropic 3D resolution further improves delineation of fine structures of the brain [10], thereby facilitating accurate deformation matching. In this work we concentrated on the investigation and optimization of isotropic 3D acquisitions by comparing two basic sequence types, namely $T_2$-weighted TSE-based sequences and SSFP-based sequences with typically mixed $T_2/T_1$ contrast.

All 3D data sets were acquired in transverse orientation relative to the rodent head, which corresponds to a coronal orientation relative to the coordinate system of the scanner.

### *Grey and white matter contrast*

Already at field strenghts of 3 T $T_1$-weighted imaging is not the contrast of choice for optimal grey and white matter differentiation. Additionally, the grey-white tissue CNR of $T_1$-weighted FLASH sequences is rather low at the intended resolutions (e.g., compare the grey-white tissue contrast in Fig. 5d). Consequently, this sequence comparison focuses on more promising sequences like TSE and SSFP.

*Turbo spin-echo sequences* TSE sequences acquire an adjustable number of *k*-space lines (so-called turbo factor, TF) for each RF excitation of the spin system by employing additional refocusing RF pulses to generate spin-echoes that are differently phase encoded [11]. While high turbo factors allow fast data acquisition, the resulting images suffer from blurring due to the $T_2$ signal decay during the multi-echo read-out period. Lower turbo factors reduce this blurring, but lengthen the acquisition time.

With the 3 T whole-body scanner being designed for human use, the system strictly limits the specific absorption rate (SAR) based on digital models applicable to humans. One possibility to reduce the SAR load with TSE sequences is the use of so-called hyperechoes [12], which is the application of varying flip angles, e.g. $\alpha = 60\ldots\ 120°$, along the refocusing rf pulse train. High flip angles are used for sampling the center of *k*-space, while lower flip angles are utilized for the acquisition of peripheral parts of *k*-space.

To achieve identical $T_2$ contrast, longer echo times have to be used compared to conventional TSE sequences with 180° refocusing pulses due to stimulated echo contributions [13]. On the other hand, the necessary lengthening of echo time in combination with refocusing flip angles as low as approximately 30°, allows one to construct TSE sequences with extremely long echo trains for 3D single-slab imaging within short acquisition times [14, 15].

Further optimizations of this approach with respect to the point spread function to reduce image blur caused by the $T_2$ signal decay [16, 17] have led recently to the development of a class of 3D sequences that have been dubbed by the acronym SPACE (Sampling Perfection with Application optimised Contrast using different flip angle Evolutions) [18].

Since both conventional 3D TSE implementations with optional hyperechoes and optimised 3D-TSE (SPACE) sequences [18, 19] are available on the MR system used here, several different TSE-based sequences were applied in the experiments whose parameters are listed in Table 1.

*bSSFP sequences* These sequences are typically very signal efficient and fast, but may suffer from banding artifacts if the local field inhomogeneities cause too large phase shifts during one $T_R$ period [20, 21]. One obvious way to reduce the banding artifacts is to keep $T_R$ as short as possible. However, due to the limited gradient strength available on a clinical system, the duration of readout gradients, and therefore echo spacing and $T_R$ are relatively long for small animal imaging applications. To remove the resulting banding artifacts, phase cycling, as used in CISS sequences [22], can be employed. However, the Siemens implementation of CISS is optimized for fluid contrast and to optimize the grey-white matter contrast two runs of a standard bSSFP sequence (TrueFISP) were used. The first repetition of the TrueFISP sequence was run with automatic frequency adjustment, the second repetition was run with a frequency offset corresponding to a phase shift of $\pi$. The scan parameters of the SSFP sequence are listed in Table 1 and additionally, a spectrally selective fat saturation preparation pulse was used. The resulting multiple images were combined by a maximum intensity projection (MIP).

*Pushing the SNR limit* To fathom hardware and SNR limitations additional SPACE and SSFP scans with increased isotropic spatial resolution of $(0.19\ \text{mm})^3$ were performed on rat brains using the Litz coil. These sequences are denoted as SPACE HR and SSFP HR in Table 1. To recover partially the loss in SNR due to smaller voxel size (factor 5.2), the number of averages (NEX) was increased. Accordingly, acquisition times increased quite drastically (see Table 1) to 80 min for the

**Table 1** Sequence parameter summary of the different sequences used in this study

| | 3D $TSE_1$ | 3D $TSE_2$ | SPACE | SPACE HR | SSFP | SSFP HR | $T_1$-weighted GRE |
|---|---|---|---|---|---|---|---|
| Isotr. resol. (mm) | 0.33 | 0.33 | 0.33 | 0.19 | 0.33 | 0.19 | 0.2 |
| Matrix | 192 × 130 × 96 | 192 × 130 × 96 | 192 × 130 × 96 | 320 × 260 × 160 | 192 × 156 × 96 | 320 × 260 × 160 | 256 × 240 × 78 |
| FoV (mm) | 64 × 43 × 32 | 64 × 43 × 32 | 64 × 43 × 32 | 62 × 50 × 30.4 | 64 × 52 × 32 | 62 × 50 × 30.4 | 54 × 53 × 14 |
| NEX[b] | 1 | 1 | 2 | 4 | 2/2[b] | 2/4[b] | 6 |
| bandwidth (*Hz/px*) | 130 | 130 | 145 | 145 | 130 | 145 | 444 |
| α (°)[a] | 180 | var. (min 60) | var. | var. | 70 | 70 | 22 |
| PF slice | 7/8 | 7/8 | 7/8 | 7/8 | 7/8 | 7/8 | 8/8 |
| PF phase | 7/8 | 7/8 | 7/8 | 7/8 | 7/8 | 7/8 | 8/8 |
| TF | 19 | 19 | 67 | 87 | – | – | – |
| ESP (ms) | 16.3 | 16.3 | 10.7 | 12.5 | 9.9 | 11.2 | – |
| $T_R$ (ms) | 2,500 | 2,500 | 2,500 | 2,500 | 528 | 3,039 | 16 |
| $T_E$ (ms) | 81 | 81 | 352 | 376 | 4.1 | 4.8 | 6.51 |
| $T_A$ (min) | 28.6 | 28.6 | 14.1 | 80 | 11.8 | 65 | 30 |

[a] For TSE-based sequences the flip angle of the refocusing RF pulses, for SSFP the steady state excitation flip angle

[b] For the SSFP sequence the NEX values have two entries, the first is the number of repetitions which are averaged for SNR improvement, the second is the number of phase cycles used. NEX denotes number of excitations (averages), *PF* Partial Fourier, *TF* turbo factor, *ESP* echo spacing, *FoV* field of view, *HR* high resolution protocols

SPACE HR. For the SSFP HR sequence four phase cycling offsets $\Delta\Phi = 0, \pi/2, \pi, 3\pi/2$ were used with two repetitions each, resulting in a total measurement time of 65 min.

### *Contrast enhanced $T_1$-weighted MRI*

While, on the one hand, $T_1$-weighted sequences are not the first choice for grey and white matter differentiation they are, on the other hand, a very good choice for contrast enhanced imaging, providing good contrast between enhancing structures and non-enhancing tissue. In this study, scans were performed to delineate the visual projection of mice using manganese enhanced MRI (MEMRI), as described in "Mouse model". An rf-spoiled, 3D GRE sequence was run with almost isotropic resolution of 0.21 × 0.22 × 0.18 mm. Further sequence parameters can be found in Table 1.

## Animal models

Animal interventions and MRI scans were performed in accordance to the European Convention for Animal Care and Use of Laboratory Animals and were approved by the local ethics committee.

### *Rat model*

Deformation-based morphometry (DBM) [23, 24] is one application where optimal grey-white matter contrast is essential for the registration process. To induce detectable volume changes in animals, a cortical malformation model [25] was used in rats to monitor cerebral volumetric changes with MRI. The coil and sequence performance was analyzed with a single healthy rat for all three coils and regular and high resolution sequences in three separate scan sessions. To verify that the image quality is sufficient for morphometric analysis of small volume changes a group analysis was performed ($n = 7$ lesioned, $n = 8$ control) at an age of 3 and 26 months.

### *Mouse model*

Manganese chloride ($MnCl_2$) enhanced MRI (MEMRI) is an established method to investigate isolated fiber projections in animals [26–29]. Acting like a biological calcium ($Ca^{2+}$) analog, manganese is incorporated in neurons by voltage-gated calcium channels and actively transported along intact microtubules of the axonal cytoskeleton, whereas passive diffusion into tissue is supposed to be negligible. Manganese propagation is interrupted in injured axonal trajectories which, in turn, allows direct observation of the vitality of axons.

As an established lesion model of the CNS, unilateral crush injury of the optic nerve (axonotmesis), which disrupts the axonal fascicles but preserves the continuity of the myelin sheaths, was applied [29, 30]. Young adult (≈120 days of age, male) C57Bl/6 mice received an intraocular injection of 2 µl of sterile 150 nmol/l$MnCl_2$/$H_2O$

solution by using a 34G needle connected to a 5 µ*l* Hamilton syringe. The $MnCl_2$ dose was determined from application protocols for rats [31] and own pharmacokinetic studies performed in mice only recently [29]. Reproducible puncture of the eye bulb was performed in the infero-temporal scleral circumference, approximately 1 mm distant from the limbus, thereby sparing scleral vessels. To monitor needle placement, liquid inoculation and eye turgor, microinjections were accomplished under a binocular microscope.

Unilateral crush injury of the right optic nerve was executed immediately before tracer application by mechanically squeezing the *N.* opticus between the tilted branches of a small forceps directly behind the posterior eye pole for 10 seconds. Deep anaesthesia was achieved by weight-adapted intraperitoneal injection of a sterile 5% chloral hydrate/PBS solution (420–450 mg/kg body weight). Additionally, liquid conjucain (0.4%) was applied to the cornea prior to the eye puncture. To prevent ocular infections and drying of the eye, ofloxacine containing eye drops and ointment were applied once.

High-resolution, $T_1$-weighted 3D MRI (see Table 1) was conducted 24 h after injection to allow sufficient time for manganese to propagate along the retino-tectal projection [29, 30]. A region of interest (ROI)-based analysis was performed to compare the left and right visual projection, expecting to see manganese induced signal enhancement along the intact side and no manganese propagation beyond the region of axonotmesis.

### Signal and contrast to noise ratio

To compare the coils and sequences both signal to noise ratio (SNR) and contrast to noise ratio (CNR) were calculated. SNR is defined as the mean signal $\overline{M}$ in a region of interest (ROI) devided by the standard deviation of the noise. Since in MR images the noise's standard deviation in a signal region can only be determined directly in homogeneity phantoms, the noise has to be estimated. For this estimation a ROI was placed in an artifact free, non-signal region, which in this evaluation were the image corners left and right of the animal's snout. The standard deviation $\sigma_b$ in this background ROI is an estimate for the noise in the image. However, due to the fact that this measure was taken from magnitude images, a correction factor of 1.53 had to be applied [32, 33] to calculate the true SNR:

$$\mathrm{SNR} = \frac{\overline{M}}{1.53 \cdot \sigma_b}. \quad (1)$$

Using the mean signal in two regions of interest $(\overline{M}_1, \overline{M}_2)$ CNR is accordingly defined as:

$$\mathrm{CNR} = \frac{(\overline{M}_1 - \overline{M}_2)}{1.53 \cdot \sigma_b}. \quad (2)$$

## Results

### MR imaging

#### *Optimal grey and white matter contrast in rat brain*

*Coil comparison* Image quality and, in particular, grey and white matter contrast was compared between the three different coils used with the rat study. Since repositioning of the animal was necessary with each coil, slice positions in the Figures shown below are not identical, although care was taken to achieve similar positions. As an example, Fig. 2 shows images of the same animal that were obtained with the same sequence (SPACE) but different coils.

The results of the corresponding ROI-based analysis are summarized in Table 2. Signal ROIs were drawn both on the original transverse images of the data sets as well as on the reformatted coronal images (Fig. 2). On transverse slices, ROIs were placed bilaterally along the cortical grey matter in rostro-caudal direction (total of 8 ROIs, averaged). The polygonally shaped white matter ROI was placed in the well delineated white matter of the corpus callosum.

In case of the reformatted coronal slices (Fig. 2, bottom row) the ROIs were again placed bilaterally and symmetrically in both hemispheres. Four ROI pairs were placed along the dorso-ventral direction in cortical brain, one pair in the white matter of the corpus callosum.

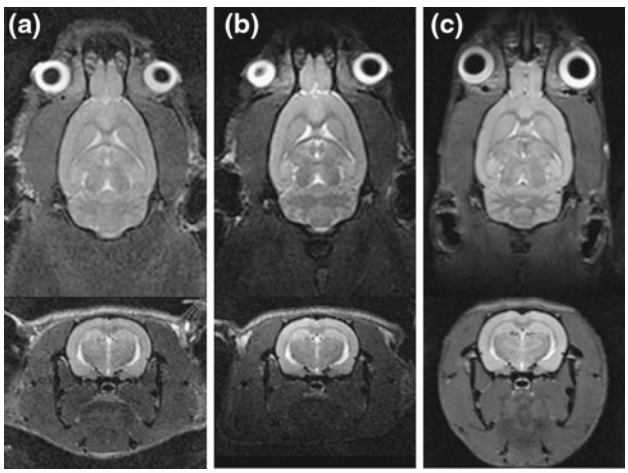


**Fig. 2** Image quality comparison of **a** CPC coil, **b** loop coil and **c** Litz coil. All three images were acquired with the SPACE sequence (NEX = 2) and the same rat, the *upper row* shows the transverse view, the *lower row* the coronal view. Angulation of the slices is not identical due to repositioning of the rat

As can be seen already in Fig. 2, the CPC coil exhibits the highest image noise but provides a homogeneous image with a large field of view. The two CPC modules, one above and one below the rat head, improved the ventral homogeneity of the image, although a SNR drop of roughly 16% remained along the dorso-ventral direction (see Table 2).

An approximately 30% improved SNR compared to the CPC coil was achieved with the small loop coil (inner diameter 30 mm) for a central brain slice. However, a distinct signal drop of about 35% was observed along the dorso-ventral direction in the brain. This signal inhomogeneity, which reflects the sensitivity profile of the single loop surface coil, can in fact be detrimental for signal intensity-based segmentation and deformation evaluations.

The Litz coil achieved a quite remarkable SNR gain of more than factor two for grey matter in comparison to the small loop coil and especially the CPC coil. This gain in SNR also translates into a substantial gain in CNR, as exemplified particularly well by the improved delineation of the fine structure of the cerebellum in Fig. 2c. Furthermore, the MR images acquired with the Litz coil were very homogeneous in both slice orientations (Fig. 2c). Grey matter signal variations were below 10% over the whole brain (see Table 2).

*Sequence comparison* Examples of the imaging results obtained with the different sequences (see Table 1) are shown in Fig. 3. The images acquired with the conventional TSE sequence ($TSE_1$) and the hyperecho TSE sequence ($TSE_2$) both suffer from blurring (Fig. 3a, b) despite the use of a moderate turbo factor of TF = 19. Though both TSE sequences achieved reasonable SNR of 53 and 58 and CNR of 7.2 and 7.8, respectively (Table 3), the SPACE sequence (Fig. 3c) not only produced sharper and more crispy images, but also provided higher SNR and a remarkably improved CNR of 22. Taking into account that the SPACE sequence, compared to the TSE sequences, requires only one third of the acquisition time, the SPACE sequence clearly outperforms the latter, yielding superior grey and white matter contrast. Reducing the acquisition time of the TSE sequence by setting $T_R$ to 1,000 ms ($T_A$ = 11 min) produced images in which contrast between grey and white matter was completely lost (results not shown). To compensate this additional $T_1$-weighting a magnetization restore pulse at the end of the echo train ($\approx$300 ms) is not successful, since after 300 ms the tissue magnetization is mostly $T_2$-decayed.

Figure 3d shows the combined image of the two phase cycled echoes of the SSFP sequence. Some residual banding artifacts are still visible, though the overall image quality appears visually acceptable with regard to grey and white matter delineation. However, comparison with the SPACE image in Fig. 3c as well as the quantitative ROI

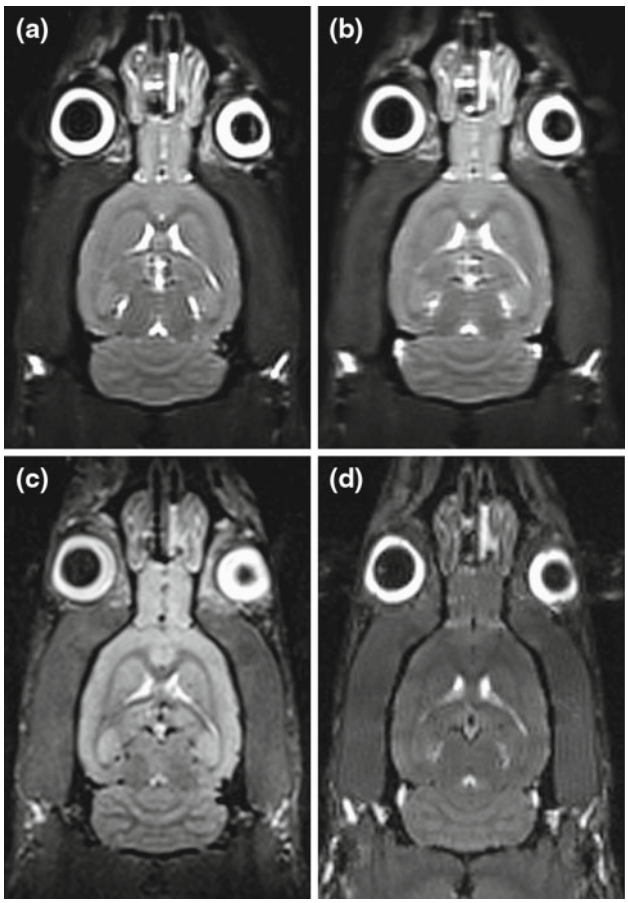


**Fig. 3** Image quality comparison of four different sequences (Table 1) for optimal *grey white* matter contrast: **a** $TSE_1$ with 1 average, **b** $TSE_2$ with 1 average, **c** SPACE using 2 averages and **d** SSFP with two phase cyclings (0, $\pi$) and 2 averages. All images are acquired in one session using the same rat, identical slice positions and the Litz coil

**Table 2** SNR and CNR coil comparison summary for rat brain imaging

| | ROI[a] | CPC | Loop | Litz |
|---|---|---|---|---|
| Trans. | $SNR_g$ | 24 | 31 | 62 |
| | $SNR_w$ | 18 | 22 | 41 |
| | CNR | 6.2 | 9.8 | 22 |
| Coron. | $SNR_g$ (surface) | 21 | 41 | 63 |
| | $SNR_g$ (center) | 19 | 31 | 57 |
| | $SNR_g$ (deep) | 18 | 26 | 59 |
| | $SNR_w$ (surface) | 14 | 26 | 42 |
| | CNR (surface) | 7.2 | 14 | 21 |

[a] SNR and grey and white matter CNR in the top part of the table were determined in a central transverse slice (see Fig. 2, top row), values in the bottom part of the table on coronal slices (Fig. 2, bottom row). All data were acquired using the same rat and identical sequence parameters

**Table 3** SNR and CNR comparison of the different sequences

| | $TSE_1$ | $TSE_2$ | SPACE | SSFP | SPACE HR | SSFP HR |
|---|---|---|---|---|---|---|
| SNR grey | 53 | 58 | 62 | 39 | 11 | 16 |
| SNR white | 46 | 50 | 41 | 31 | 8.1 | 14 |
| CNR | 7.2 | 7.8 | 22 | 7.2 | 3.3 | 2.7 |

evaluation revealed significantly reduced grey and white matter contrast of the SSFP sequence.

*Pushing the SNR limit* Data acquisition with both the high resolution protocols SPACE HR and the SSFP HR (Table 1) resulted in images as shown in Fig. 4. With the increased isotropic spatial resolution of $(0.19\ \text{mm})^3$ smaller structures became visible and more details, e.g. in the cerebellum, were more clearly delineated, particularly with the SPACE HR sequence. SNR and CNR of the SPACE HR and the SSFP HR sequence were similar (see Table 3), although CNR values became rather low at this resolution (3.3 and 2.7, respectively), impeding application for reliable tissue segmentation. One interesting finding was that the water signal was effectively suppressed in the SPACE HR image while water was still bright in the SSFP HR image. Additionally, the SNR performance of the SPACE HR sequence dropped much stronger than that of the SSFP HR and was in fact lower than in the SSFP HR sequence. Compared to the SNR of the lower resolution SPACE and SSFP sequence this is a quite surprising SNR loss.

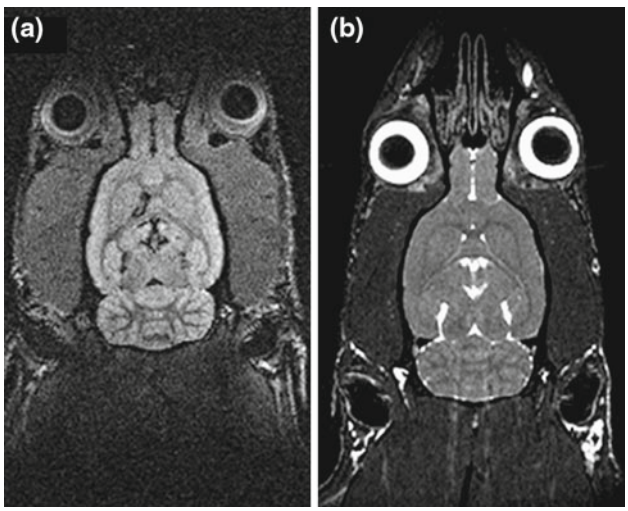


**Fig. 4** Transverse slice of rat brains using the Litz coil at an isotropic resolution of $(0.19\ \text{mm})^3$. **a** SPACE HR sequence using 4 averages with total acquisition time of 80 min. **b** SSFP HR sequence using 2 repetitions and 4 echoes with phase shifts of 0, $\pi/2$, $\pi$, $3\pi/2$ and a total acquisition time of 65 min

*Contrast enhanced $T_1$-weighted MRI*

Results of the high spatial resolution MR acquisition of the intact retino-tectal projection in mice following $MnCl_2$ injection are compared in Fig. 5 for the phased-array whole-body mouse coil (Fig. 5a) and the Litz coil (Fig. 5b, c). Neuroanatomic centers of the retino-petal projection including the ipsilateral retinal ganglion cell axons forming the optic nerve, their fiber crossover in the optic chiasm, and the contralateral thalamic LGN and midbrain SC were clearly depicted in these reconstructed maximum intensity projections. Distinct focal manganese uptake was specifically discernible along the intact pathway while lacking intracerebrally along the injured site. In comparison, the Litz coil provided superior image quality to the phased-array mouse coil (Fig. 5). The detected pattern of enhanced signal proved to be highly specific.

SNR and CNR were determined from single slices obtained from the same animal (see Fig. 5d). The two signal ROIs for the calculation of the CNR were placed in projection-specific enhancing areas and non-enhancing brain tissue. The results are summarized in Table 4.

## Discussion

### Grey and white matter contrast

High resolution structural animal brain MRI is fundamentally limited by SNR. To attain signal optimum at clinical field strengths, specially tailored coils have to be used. While the simple loop design is often considered to be the most SNR efficient variant [6], it exhibits a strong signal dependency with distance $r$ from the coil center ($\propto 1/r^2$). This signal dependency causes strong signal variations across images, as shown in Fig. 2 and Table 2. Consequently, it can pose a problem for threshold-based tissue segmentation and can also be problematic for intensity-based deformation algorithms.

Also, due to this more or less inhomogeneous signal distribution of the coils, a single SNR value is not the whole truth. In phantoms, depending on the ROI placement, SNR variations of 50% and larger could be measured. However, a coil's excellent SNR performance in a particular region is only of help, if a region of interest can actually be placed there. Real world examples as the cortical grey-white matter contrast in rats or the visual projection in mice, as demonstrated here, give a better idea of a coil's performance for that particular application, and Table 2 details the spatial SNR and CNR dependency in two orientations.

Although normalisation filters and use of prescans and coil sensitivity maps help to achieve homogeneous signal

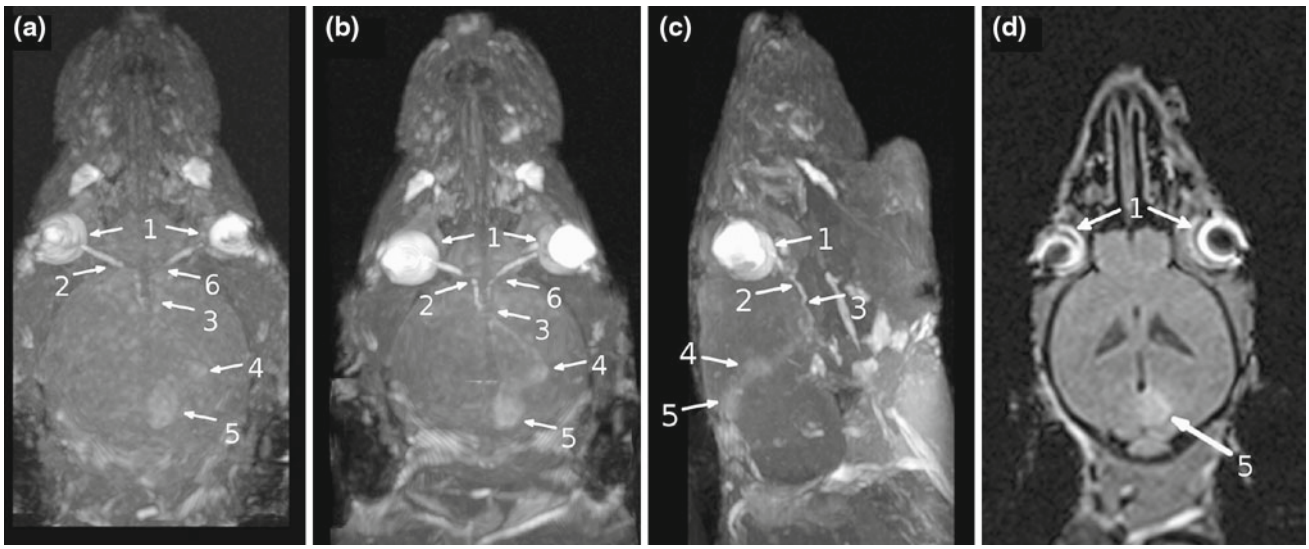


**Fig. 5** MEMRI mouse images: **a–c** show coronal (**a**, **b**) and saggital (**c**) MIP images of the mouse brain acquired with the 8-channel phased-array mouse coil (**a**), and the rat head Litz coil (**b**, **c**). The $Mn^{2+}$ enhanced intact visual pathway is best visible by acquisition with the Litz coil (**b**, **c**). Note the lack of contralateral thalamic and midbrain signals (*4*, *5*) distal to the injured optic nerve (*6*). The *arrows* mark (*1*) retina, (*2*) intact optic nerve, (*3*) chiasm, (*4*) lateral geniculate nucleus (LGN), (*5*) superior colliculus (SC) and (*6*) the crushed optic nerve. Obstructing ventral anatomical features (**c**) were cropped for both coronal images (**a**, **b**). Gamma correction was applied to all MIP images. (**d**) Shows a single slice containing retina (*1*) and SC (*5*) of the image data acquired with the Litz coil. The *arrows* mark the anatomical regions correspondig to the ROIs used for Table 4

across the image, SNR will nevertheless remain low in low signal regions. Thus, the problem of inhomogeneous signal is only shifted to inhomogeneous SNR and/or CNR, both of which are detrimental to morphometric analysis.

The signal homogeneity of loop coils can be improved by using larger loops, which increases the penetration depth, but also reduces SNR, as demonstrated by the inferior SNR performance of the CPC coil compared to the Loop coil. Performing imaging with a dedicated rat head coil with a Litz volume resonator [6] improved SNR substantially. In this work, the gain in SNR was roughly twofold compared to the Loop coil. The necessary image quality to morphometrically detect local volume changes can be achieved with all three coils at the expense of acquisition time (e.g., NEX = 6 for the CPC coil). However, the Litz coil with its improved intrinsic SNR allows scan times on the order of 10–15 min and therefore a very high throughput for animal studies.

The SPACE sequence clearly provided the best image quality per measurement time. While the SSFP sequence provided also good SNR, the $T_2/T_1$-weighting of the SSFP sequence reduced the grey and white matter contrast, which is essential for morphometry. The SPACE sequence is one example of highly advanced clinical sequences, which have no direct correspondence on typical small animal scanners. The ready availability of this 3D-optimised TSE variant is a clear advantage of the clinical scanner.

Subsequent DBM analysis of the acquired MR data sucessfully detected significant volume differences at the freeze lesion site between the rat malformation model and the controls. In aged, lesioned animals further localized atrophy could be detected, which confirms that the SPACE images provide the necessary resolution to detect small volume changes.

**Table 4** SNR and CNR comparison of manganese enhancing areas of the retino-petal projection of a mouse

| | 8-ch mouse coil | | Litz coil | |
|---|---|---|---|---|
| ROI region | Crush | Intact | Crush | Intact |
| SNR retina (1) | 19 | 25 | 46 | 52 |
| SNR N. opt. (2) | 20 | 27 | 43 | 63 |
| SNR LGN (4) | 17 | 22 | 33 | 42 |
| SNR SC (5) | 17 | 21 | 34 | 45 |
| CNR retina (1) | 3.3 | 8.3 | 12 | 18 |
| CNR N. opt. (2) | 5.0 | 11 | 9.9 | 30 |
| CNR LGN (4) | 2.2 | 6.5 | 2.8 | 11 |
| CNR SC (5) | 1.0 | 5.9 | 2.7 | 12 |

Numbers (1–5) in ROI nomenclature correspond to the marked areas in Fig. 5

The excellent image quality and the relatively short scan time of the SPACE sequence encouraged us to further increase the resolution. However, increasing the resolution to $(0.19\ \text{mm})^3$ reduced SNR due to the smaller voxel volume and increased acquisition time for a single repetition to 20 min due to the larger imaging matrix. To fully compensate the SNR loss by averaging would require approximately 9 hours of data acquisition. On the other

hand, it has recently been reported that an SNR of 10[1] [34] to 20 [35] is the optimal trade off between resolution and SNR. This is, in fact, reflected in the SPACE HR and SSFP HR images (Fig. 4), which show distinctly more details compared to the images shown in Fig. 3(c, d) and have an SNR which is close to the proposed optimal SNR (see Table 3).

Some interesting observations were made when the resolution of the SPACE and SSFP sequence was increased to $(0.19\ \text{mm})^3$ voxel size. As described in the results section, SNR and CNR of the SPACE HR sequence became very similar to that of the SSFP HR sequence (see Table 3) and the water signal was drastically reduced in the SPACE HR images. The SSFP HR images, on the other hand, depict water still with hyperintense signal. Since the excitation and refocusing pulses of the SPACE sequence are non-selective, this effect cannot be explained by flow-voids, as commonly seen with 2D-TSE sequences.

This water suppression most probably arises from accumulating diffusion weighting [36] due to the stronger and longer read-out and phase encode gradients in combination with a higher turbo factor. The imaging gradients in the SPACE sequence comprise symmetric pairs of dephasing and rephasing gradient pulses within each $T_R$, which act as small diffusion sensitising gradients. The diffusion effect is less pronounced in the steady-state of an SSFP sequence, which consists of a mixture of fresh FID components with previous, rephasing echo components, whereas the SPACE sequence uses the initial magnetization and splits it into a series of components decaying with either $T_1$ or $T_2$ depending on their longitudinal or transverse magnetization state [13, 36]. In the SPACE sequence, the FID components are explicitly spoiled by crusher gradients, and only the initial 90°-excited magnetization contributes to the imaging signal. Therefore, for the SPACE HR sequence, the diffusion weighting effects of the strong imaging gradients accumulate over the full echo train length (TF = 87), which explains the relative SNR loss compared to the SSFP sequence. Although this diffusion weighting effect of the SPACE sequence acts strongest on free water, brain tissue signal is reduced as well.

Even with the resolution pushed to the SNR limit, the SPACE sequence's images were very sharp and provided good contrast. Further optimization of the SPACE sequence, for example by extended phase graph simulations [36], might be able to minimize the diffusion weighting effect. Alternative sequences, like SSFP, may provide better SNR and bright water signal for anatomic delineation, but require proper handling of the banding artifacts [37].

[1] Original paper states an SNR of 16, but the SNR calculation from magnitude images does not include the correction factor of Eq. 1.

### $T_1$-weighted contrast (MEMRI mouse model)

Manganese enhanced $T_1$-weighted MR imaging of the mouse model delineated the visual pathway very clearly. However, there are large signal differences between retina and the more diffuse enhancements of the thalamic and midbrain centers. Care had to be taken to avoid clipping in the high intensity regions like retina and compact optic nerve. Nevertheless, in spite of these considerable signal differences, this technique succeeds in selective and quantitative measurements of contrasting effects along a specific fiber projection within the mouse brain.

One potential problem that can occur with *in-vivo* $T_1$-weighted, short TR MRI was coincidentally avoided when using the 8-channel mouse coil (body coil transmit) or the Litz volume resonator. With both coils, the RF excitation pulses cover a large part of the mouse body, including breast and heart as well as the whole head. As a consequence, inflow effects of major (arterial) blood vessels are strongly suppressed. Otherwise, these vessels would produce bright signal, as is utilized in MR time-of-flight (TOF) angiography, which employs the very same sequences, and would overlay the manganese enhancement pattern making it difficult to separate both. Subtraction imaging to remove the vessels is not easily feasible, since a 24 h period is required between a native image and the post contrast image, involving a complete repositioning of the mouse.

In our measurements with the Litz coil, the inflow-enhancement effect was already noticeable due to the smaller length of the Litz coil and the concomitant smaller saturation volume. Intradural segments and branches of the ophthalmic artery that run within the optic nerve sheath were difficult to separate from the adjacent optic nerve itself. This inflow signal was completely suppressed using the 8-channel coil for signal reception together with the scanner's body coil serving as transmitter.

Further improvements in SNR by a factor of 2 are to be expected when replacing the Litz rat head coil with a more dedicated scaled-down mouse head coil with the same Litz configuration. However, with the smaller excitation volume of a mouse head coil, suppression of in-flow effects will be less efficient. Using a Litz coil in receive-only mode in combination with body coil excitation pulses might be advantageous for MEMRI in that case.

### Fundamental limitations on clinical scanners

One major limitation of small animal imaging on clinical scanners is the limited shim capability. The automatic 3D shim procedures offered by the clinical systems are typically based on full FoV (500 mm) images, on which a rat or mouse brain is represented at most by just a few voxels. A calculated shim set based on these images is not very

useful, and consequently the scanner's default setting ("tune up") was loaded and used for all experiments.

The spin-echo-based sequences are usually sufficiently robust against off-resonance effects to tolerate suboptimal shims. With the SSFP sequence, manual shimming was performed based on gradient echo phase images that were acquired with an appropriately adjusted FoV. As it turned out, one linear axial shim component was sufficient to remove the worst part of field inhomogeneities in the rats', and especially in the mice's brains. The higher order shim components were actually not helpful due to the limited shim gradient power available.

Ultrafast sequences like EPI, which are extremely sensitive to off-resonance effects, are of very limited use for rats and not suitable for mice, not only because of the shim issues but also because of the limited gradient power and slew rates that are necessary for small FoV imaging. For high resolution gradient echo imaging, on the other hand, off-resonance effects and field inhomogeneities cause primarily intravoxel dephasing, which is strongly suppressed by the small isotropic voxel size. Limited $T_2^{\star}$-weighted imaging is therefore possible, e.g., with rf-spoiled, gradient-echo-based sequences.

One hardware limitation is concerned with the coils. Even with the coil size well adapted to the size of a mouse and the small surface elements being in close vicinity to the animal, the SNR performance of the 8-channel mouse coil could not compete with the single channel Litz volume resonator. For very small objects, like rat and certainly mouse heads, the noise is no longer dominated by physiological and thermal object noise but by noise from the electronic pathways [38]. Therefore, more channels may also introduce more noise. Consequently, if the whole body capability of the 8-channel mouse coil ist not needed, a smaller loop or Litz design offers better SNR performance. However, the multi channel coil offers parallel imaging capabilities which would be essential to attempt EPI in mice.

## Conclusions

Anatomical grey and white matter contrast MR imaging with high spatial resolution of rat brains was successfully performed on a clinical 3 T whole body scanner. Although conventional 3D TSE sequences, with or without application of hyperechoes, provided acceptable image quality and grey white contrast, the measurement times were considerably longer than for the SPACE and SSFP sequences. In particular, the SPACE sequence provided the best CNR between grey and white matter and achieved remarkably sharp image quality compared to the TSE variants.

Both the SPACE as well as the SSFP proved sufficiently robust against geometric distortions even in areas of steep magnetic field gradients at the air-tissue boundaries. The banding artifacts of the SSFP sequence were successfully removed using phase cycling acquisition.

To achieve the necessary SNR performance on a clinical 3 T scanner the use of small coils is essential. In our comparison the dedicated small animal coils had a significant SNR advantage over larger multipurpose coils. The SNR of brain images obtained with the 8-channel array was inferior compared to the Litz volume resonator, most likely due to electronic noise dominating over the object noise.

An isotropic spatial resolution of $(0.33\ \mathrm{mm})^3$ can be achieved on clinical scanners within short scan times, making longitudinal, structural and morphological investigations with high throughput of rodents quite feasible. By increasing the scan time to 30–60 min, even resolutions of 0.2 mm are achievable with sufficient image quality. Further optimization of coil design and sequences may push this limit even further.

**Acknowledgments** We thank Noras MRI products GmbH and Siemens Medical for their support and the mechanical workshop of the Friedrich-Schiller University Jena for their help in creating the various head holders.

## References

1. Boretius S, Kasper L, Tammer R, Michaelis T, Frahm J (2009) MRI of cellular layers in mouse brain in vivo. Neuroimage 47:1252–1260
2. Pinkernelle JG, Stelter L, Hamm B, Teichgraber U (2008) Small animal MRI: clinical MRI as an interface to basic biomedical research. Rofo 180:505–513
3. Chronik B, Alejski A, Rutt BK (2000) Design and fabrication of a three-axis multilayer gradient coil for magnetic resonance microscopy of mice. Magn Reson Mater Phys 10:131–146
4. Linn J, Schwarz F, Schichor C, Wiesmann M (2007) Cranial MRI of small rodents using a clinical MR scanner. Methods 43:2–11
5. Gareis D, Behr VC, Breuer F, Griswold M, Jakob P (2006) Multipurpose 4+4 channel array setup for parallel imaging in 3D. In Proceedings 14th scientific meeting, international society for magnetic resonance in medicine, p 499
6. Doty FD, Entzminger G, Kulkarni J, Pamarthy K, Staab JP (2007) Radio frequency coil technology for small-animal MRI. NMR Biomed 20:304–325
7. Herrmann KH, Wagner E, Deistung A, Hilger I, Reichenbach JR (2008) A robust optical respiratory trigger for small rodents in clinical whole-body MR systems. Biomed Tech (Berl) 53:138–144
8. Schubert MI, Porkess MV, Dashdorj N, Fone KC, Auer DP (2009) Effects of social isolation rearing on the limbic brain: a combined behavioral and magnetic resonance imaging volumetry study in rats. Neuroscience 159:21–30
9. Gaser C, Nenadic I, Buchsbaum BR, Hazlett EA, Buchsbaum MS (2001) Deformation-based morphometry and its relation to conventional volumetry of brain lateral ventricles in MRI. Neuroimage 13:1140–1145
10. Natt O, Watanabe T, Boretius S, Radulovic J, Frahm J, Michaelis T (2002) High-resolution 3D MRI of mouse brain reveals small cerebral structures in vivo. J Neurosci Methods 120:203–209

11. Hennig J, Nauerth A, Friedburg H (1986) RARE imaging: a fast imaging method for clinical MR. Magn Reson Med 3:823–833
12. Hennig J, Scheffler K (2001) Hyperechoes. Magn Reson Med 46:6–12
13. Weigel M, Hennig J (2008) Development and optimization of T2 weighted methods with reduced RF power deposition (Hyperecho-TSE) for magnetic resonance imaging. Z Med Phys 18:151–161
14. Horger W, Kiefer B, Menzel M, Mugler III J P (2006) Efficient phase-encoding for 3D turbo-spin-echo imaging with very long echo trains. In Proceedings 14th scientific meeting, international society for magnetic resonance in medicine, p 2429
15. Mugler III JP (2007) Signal and contrast properties of very-long spin-echo trains for 3D T2-weighted turbo-spin-echo imaging. In Proceedings 15th scientific meeting, international society for magnetic resonance in medicine, p 794
16. Hennig J, Weigel M, Scheffler K (2004) Calculation of flip angles for echo trains with predefined amplitudes with the extended phase graph (EPG)-algorithm: principles and applications to hyperecho and TRAPS sequences. Magn Reson Med 51:68–80
17. Park J, Mugler JP, Hughes T (2009) Reduction of B1 sensitivity in selective single-slab 3D turbo spin echo imaging with very long echo trains. Magn Reson Med 62:1060–1066
18. Lichy M P, Wietek B, Mugler III JP et al (2005) Whole-body applications of isotropic high-resolution T2-weighted MRI with a single-slab 3D-TSE-based sequence optimized for high sampling efficiency, called SPACE—initial clinical experiences. In Proceedings 13th scientific meeting, international society for magnetic resonance in medicine, p 794
19. Busse RF, Brau AC, Vu A, Michelich CR, Bayram E, Kijowski R, Reeder SB, Rowley HA (2008) Effects of refocusing flip angle modulation and view ordering in 3D fast spin echo. Magn Reson Med 60:640–649
20. Carr HY (1958) Steady-state free precession in nuclear magnetic resonance. Phys Rev 112:1693–1708
21. Sobol WT, Gauntt DM (1996) On the stationary states in gradient echo imaging. J Magn Reson Imag 6:384–398
22. Casselman J W, Kuhweide R, Deimling M, Ampe W, Dehaene I, Meeus L (1993) Constructive interference in steady state-3DFT MR imaging of the inner ear and cerebellopontine angle. AJNR Am J Neuroradiol 14:47–57
23. Gaser C, Volz HP, Kiebel S, Riehemann S, Sauer H (1999) Detecting structural changes in whole brain based on nonlinear deformations-application to schizophrenia research. Neuroimage 10:107–113
24. Lau JC, Lerch JP, Sled JG, Henkelman RM, Evans AC, Bedell BJ (2008) Longitudinal neuroanatomical changes determined by deformation-based morphometry in a mouse model of Alzheimer's disease. Neuroimage 42:19–27
25. Schmidt S, Bruehl C, Hagemann G, Witte OW, Redecker C (2006) Impairment of functional inhibition in the contralateral cortex following perinatally acquired malformations in rats. Exp Neurol 201:270–274
26. Bearer EL, Falzone TL, Zhang X, Biris O, Rasin A, Jacobs RE (2007) Role of neuronal activity and kinesin on tract tracing by manganese-enhanced MRI (MEMRI). Neuroimage 37(suppl 1): 37–46
27. Chan KC, Fu QL, So KF, Wu EX (2007) Evaluation of the visual system in a rat model of chronic glaucoma using manganese-enhanced magnetic resonance imaging. Conf Proc IEEE Eng Med Biol Soc 2007:67–70
28. Thuen M, Berry M, Pedersen TB, Goa PE, Summerfield M, Haraldseth O, Sandvig A, Brekken C (2008) Manganese-enhanced MRI of the rat visual pathway: acute neural toxicity, contrast enhancement, axon resolution, axonal transport, and clearance of Mn(2+). J Magn Reson Imag 28:855–865
29. Haenold R, Herrmann KH, Schmidt S et al (2011) Magnetic resonance imaging of the mouse visual pathway for in vivo studies of degeneration and regeneration in the CNS. Neuroimage. doi:10.1016/j.neuroimage.2011.07.069
30. Thuen M, Singstad TE, Pedersen TB, Haraldseth O, Berry M, Sandvig A, Brekken C (2005) Manganese-enhanced MRI of the optic visual pathway and optic nerve injury in adult rats. J Magn Reson Imag 22:492–500
31. Thuen M, Olsen O, Berry M, Pedersen TB, Kristoffersen A, Haraldseth O, Sandvig A, Brekken C (2009) Combination of Mn(2+)-enhanced and diffusion tensor MR imaging gives complementary information about injury and regeneration in the adult rat optic nerve. J Magn Reson Imag 29:39–51
32. Henkelman RM (1985) Measurement of signal intensities in the presence of noise in mr images. Med Phys 12:232–233
33. Kaufman L, Kramer DM, Crooks LE, Ortendahl DA (1989) Measuring signal-to-noise ratios in MR imaging. Radiology 173:265–267
34. Portnoy S, Kale SC, Feintuch A, Tardif C, Pike GB, Henkelman RM (2009) Information content of SNR/resolution trade-offs in three-dimensional magnetic resonance imaging. Med Phys 36:1442–1451
35. Kale SC, Lerch JP, Henkelman RM, Chen XJ (2008) Optimization of the SNR-resolution tradeoff for registration of magnetic resonance images. Hum Brain Mapp 29:1147–1158
36. Weigel M, Schwenk S, Kiselev VG, Scheffler K, Hennig J (2010) Extended phase graphs with anisotropic diffusion. J Magn Reson 205:276–285
37. Elliott AM, Bernstein MA, Ward HA, Lane J, Witte RJ (2007) Nonlinear averaging reconstruction method for phase-cycle SSFP. Magn Reson Imag 25:359–364
38. Baltes C, Radzwill N, Bosshard S, Marek D, Rudin M (2009) Micro MRI of the mouse brain using a novel 400 MHz cryogenic quadrature RF probe. NMR Biomed 22:834–842